Thin-Walled Structures 170 (2022) 108653

Contents lists available at ScienceDirect

Thin-Walled Structures

journal homepage: www.elsevier.com/locate/tws

Full length article

A new spectral finite element for the study of face sheet–core disbond identification in a sandwich panel

M.V.V.S. Murthy [a,*], S. Gopalakrishnan [b], D. Poomani [a]

[a] Structures Group, U R Rao Satellite Center, ISITE, ISRO, Bangalore 560037, India
[b] Department of Aerospace Engineering, Indian Institute of Science, Bangalore 560012, India

ARTICLE INFO

Keywords:
Spectral Finite Element Method
Wave propagation
Sandwich panel
High Frequency
Debond identification

ABSTRACT

A new two-node spectral finite element for a sandwich panel with 13DOF/node is formulated to study the face sheet–core disbond in a sandwich panel. The spectral element formulation results in an exact dynamic stiffness matrix for the element. The study on wave propagation characteristics for both healthy and disbonded sandwich panel is carried out. The numerical results obtained using this spectral element are validated by comparing with the results obtained through simulations using commercially available finite element software. The effect of core damping for waves propagating in both through-thickness and along the length of the panel is clearly demonstrated. The interaction of the waves propagating between the face sheet–core disbond is studied and using numerical examples it is shown that the amplitude change is a measure to identify the disbond whereas the arrival times can be used to estimate the size of the disbond.

1. Introduction

Typical sandwich structures are made of two very thin face sheets (also referred to as skins) and a thick core included between the face sheets. Due to their desirable properties like bending stiffness with low weight; they are particularly employed in aerospace and space industries. As an example, in the composite sandwich panel, thin carbon fibre reinforced face sheets are bonded to thick aluminium honeycomb core using adhesives. Defects/damage occur in sandwich panels as 'production defects' and 'in-service damage', like impact damage due to tool drop. These defects are to be identified and rectified for efficient operation of the structure. The defects in sandwich structures [1] are,

1. facesheet–core disbonds,
2. voids and inclusions in the core,
3. lack of bond (edge-to-edge and face-to-face) between core sheets.

The present study involves modelling of face sheet–core disbond and identifying this defect using guided waves. High frequency ultrasonic guided waves are employed while conducting Non-Destructive Evaluation (NDE) tests for inspecting large structures with surface defects, deeply embedded defects like delamination in composites and hidden defect like the face-sheet core disbond. This is because the guided waves propagate long distances and are sensitive to defects. One can work out the wavelength/frequency of the guided waves to be excited based on the extent of defects to be identified. Exhaustive studies using guided waves are available in the literature to identify defects in metals and composites. To demonstrate the use of low frequency Lamb waves for inspection, an experimental work is carried out to study the interaction of Lamb waves with different types of damage in monolithic and sandwich composite beams [2]. An imaging algorithm based on time reversal is developed to detect debonding in sandwich composite structures using guided ultrasonic wave signals [3]. Elastic wave propagation mechanism in aluminium skin–hexagonal Nomex core sandwich structures is investigated both numerically, through finite element (FE) simulation and experimentally by using a surface-bonded piezoelectric actuator/sensor system. In addition, the influence of cell geometry parameters upon wave propagation is discussed in [4]. Numerical simulations are conducted using commercially available finite element package, ABAQUS, in order to explore guided wave propagation mechanisms due to the presence of disbond. A good agreement is observed between the numerical and experimental results. Later, the location of an unknown disbond, within the piezoelectric wafer transducer array is experimentally determined by applying a probability-based damage detection algorithm and is presented in [5]. Similarly, using ABAQUS, a detailed finite element model for a sandwich composite panel is modelled, in order to simulate impact-induced damage formation and scattering of the acoustic waves in [6] where, the responses were compared with the experimental results, showing both to be in good agreement. The results obtained through the Finite Element Method (FEM) are validated with the results obtained through experimental studies.

* Corresponding author.
E-mail address: mvvsmurthy@gmail.com (M.V.V.S. Murthy).

https://doi.org/10.1016/j.tws.2021.108653
Received 14 August 2021; Received in revised form 31 October 2021; Accepted 2 November 2021
Available online 20 November 2021

While the FEM finds use in many commercial applications, in order to capture the response in high frequency loading, the size of the finite element should be small as compared to the wavelength, resulting in to increase in system size and high computational time for the solutions. The Spectral Finite Element Method (SFEM) compared to FEM has the merit of handling problems in the frequency domain and theoretically one element is sufficient to model problems without discontinuity. The method is well discussed for isotropic cases [7] and composite cases [8]. Identification of structural boundaries using the spectral finite element method can be found in [9]. Works on sandwich beam [10] and sandwich plate [11] problems were conducted by formulating the sandwich beam and sandwich plate in the spectral element domain. All the above mentioned spectral finite elements use Equivalent Single Layer (ESL) theories and do not capture the independent motions of the face sheets.

Later, an extended Higher-order Sandwich Panel Theory (HSAPT) is proposed in [12] and responses obtained for different static loading cases are compared with that of the elasticity solutions. In [13], wave propagation studies were carried out and the independent motions of the top and bottom face sheets were captured by formulating a spectral finite element based on HSAPT. In the HSAPT the face sheets are modelled according to Euler–Bernoulli theory and the core is modelled using Third order Shear Deformation Theory (TSDT). Both the top face sheet and bottom face sheet are connected to the core using kinematic constraints to simulate perfect bonding. Later, the HSAPT is modified by modelling the face sheets based on First-order Shear Deformation Theory (FSDT). Based on the modified HSAPT, studies on the onset and propagation of disbond mechanism is carried out for static loading case [14] and dynamic loading case [15], using the finite difference method.

Most of the spectral finite elements in the existing literature use the Fourier transform to solve the equations of motion. Fourier transform assumes that the time signal is periodic in time domain and introduce periodicity in the frequency domain to remove the integral representation of the forward transform. Signal wrap-around is observed in the time domain responses as a consequence of using the discrete inverse Fourier transform along with the induced periodicity in the frequency domain. This wrap-around can be avoided by either increasing the time window or adding sufficient damping to the response. Sometimes, a combination of both may be required. Alternatively, Laplace transform has been used to alleviate the wrap-around problem. Composite beam spectral finite element based on FSDT is developed using the Laplace transform [16] where, the numerical Laplace transform is implemented through the fast Fourier transform, retaining the excellent frequency domain analysis provided by the Fourier transform based spectral elements. As to the best of the authors'knowledge, there is no literature existing available in the public domain on a spectral finite element formulation incorporating face sheet–core disbond and there exists very limited theoretical studies using FEM.

Here, first a new spectral finite element is formulated based on the modified HSAPT. The disbond is introduced as a cohesive interface, following traction-displacement gap laws. Next, the element formulation is used to study wave propagation characteristics in a sandwich panel. Later, the developed element is validated by comparing with the results obtained through simulations using commercially available finite element software. Finally, the element is used to study the wave interactions at face sheet–core disbond in a sandwich panel and the results obtained through numerical experiments are discussed.

2. Spectral finite element formulation

The geometry of the sandwich panel is given in Fig. 1, where, f^t, f^b and $2h^c$ are the top face sheet thickness, bottom face sheet thickness and total thickness of the core respectively. The spectral finite element is formulated based on HSAPT incorporating the sandwich panel as three layers, the top face sheet (denoted with superscript 't'), the core (denoted with superscript 'c') and the bottom face sheet (denoted with superscript 'b'). FSDT is used to model the face sheets and TSDT for the core. Fig. 2 shows the interface between face sheets and core modelled using interfacial traction-displacement gap laws, along with inertial forces and concentrated forces.

2.1. Displacement field

The displacement functions for top and bottom face sheets are given as,

$$u^i(x^i,z^i,t) = u_0^i(x^i,t) - z^i\phi^i(x^i,t) \tag{1a}$$

$$w^i(x^i,t) = w_0^i(x^i,t) \tag{1b}$$

where, u_0^i is the longitudinal mid-plane displacement, W_0^i is the transverse mid-plane displacement, ϕ^i is the mid-plane rotation, the superscript i = 't' for top face sheet and 'b' for bottom face sheet, x^i is the horizontal coordinate and z^i is the vertical coordinate measured positive downwards from the respective mid-plane of the face sheets.

Similarly, the displacement field for the core is given as,

$$u^c(x^c,z^c,t) = u_0^c(x^c,t) + z^c u_1^c(x^c,t) + z^{c^2}u_2^c(x^c,t) + z^{c^3}u_3^c(x^c,t) \tag{2a}$$

$$w^c(x^c,z^c,t) = w_0^c(x^c,t) + z^c w_1^c(x^c,t) + z^{c^2}w_2^c(x^c,t) \tag{2b}$$

where, u^c is the in-plane displacement of the core, W^c is the transverse displacement of the core, x^c is the horizontal coordinate, z^c is the vertical coordinate measured positive downwards from the mid-plane of the core, u_0^c is the mid-plane displacement of the core, W_0^c is the mid-plane displacement of the core and u_1^c, u_2^c, u_3^c, W_1^c, W_2^c are the higher-order displacement functions of the core. For the sake of brevity, from here the functional dependency of all functions is not explicitly shown, as for example, $u^c(x^c,z^c,t)$ is simply written as u^c, $u_0^c(x^c,t)$ as u_0^c and so on for all displacement functions.

The strains in the face sheets are given as,

$$\{\epsilon^i\} = \begin{Bmatrix} \epsilon_{xx}^i \\ \gamma_{xz}^i \end{Bmatrix} = \begin{Bmatrix} \frac{\partial u^i}{\partial x^i} \\ \frac{\partial u^i}{\partial z^i} + \frac{\partial w^i}{\partial x^i} \end{Bmatrix} = \begin{Bmatrix} \frac{\partial u_0^i}{\partial x^i} - z^i\frac{\partial \phi^i}{\partial x^i} \\ \frac{\partial w_0^i}{\partial x^i} - \phi^i \end{Bmatrix} \tag{3}$$

and the strains in the core are given as,

$$\begin{aligned}\{\epsilon^c\} &= \begin{Bmatrix} \epsilon_{xx}^c \\ \epsilon_{zz}^c \\ \gamma_{xz}^c \end{Bmatrix} = \begin{Bmatrix} \frac{\partial u^c}{\partial x^c} \\ \frac{\partial w^c}{\partial x^c} \\ \frac{\partial u^c}{\partial z^c} + \frac{\partial w^c}{\partial x^c} \end{Bmatrix} \\ &= \begin{Bmatrix} \frac{\partial u_0^c}{\partial x^c} + z^c\frac{\partial u_1^c}{\partial x^c} + z^{c^2}\frac{\partial u_2^c}{\partial x^c} + z^{c^3}\frac{\partial u_3^c}{\partial x^c} \\ w_1^c + 2z^c w_2^c \\ u_1^c + 2z^c u_2^c + 3z^{c^2}u_3^c + \frac{\partial w_0^c}{\partial x^c} + z^c\frac{\partial w_1^c}{\partial x^c} + z^{c^2}\frac{\partial w_2^c}{\partial x^c} \end{Bmatrix}\end{aligned} \tag{4}$$

The constitutive relations for the face sheets are given as,

$$\begin{Bmatrix} \sigma_{xx}^i \\ \tau_{xz}^i \end{Bmatrix} = \begin{bmatrix} \bar{Q}_{11}^i & 0 \\ 0 & \bar{Q}_{55}^i \end{bmatrix} \begin{Bmatrix} \epsilon_{xx}^i \\ \gamma_{xz}^i \end{Bmatrix} \tag{5}$$

where, the components $\bar{Q}_{ij}^i$ are the inverse of the compliance matrix [17] and the constitutive relation for the core is given as,

$$\begin{Bmatrix} \sigma_{xx}^c \\ \sigma_{zz}^c \\ \tau_{xz}^c \end{Bmatrix} = \begin{bmatrix} \frac{E^c}{1-\nu^{c2}} & \frac{\nu^c E^c}{1-\nu^{c2}} & 0 \\ \frac{\nu^c E^c}{1-\nu^{c2}} & \frac{E^c}{1-\nu^{c2}} & 0 \\ 0 & 0 & G^c \end{bmatrix} \begin{Bmatrix} \epsilon_{xx}^c \\ \epsilon_{zz}^c \\ \gamma_{xz}^c \end{Bmatrix} \tag{6}$$

where, E^c, G^c, ν^c are the Young's modulus, the rigidity modulus and Poisson's ratio of the core.

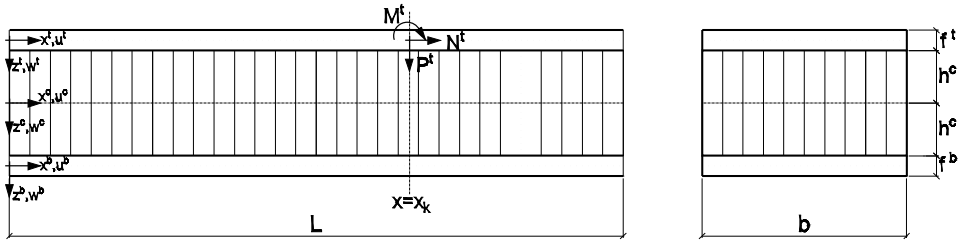

Fig. 1. Sandwich beam configuration.

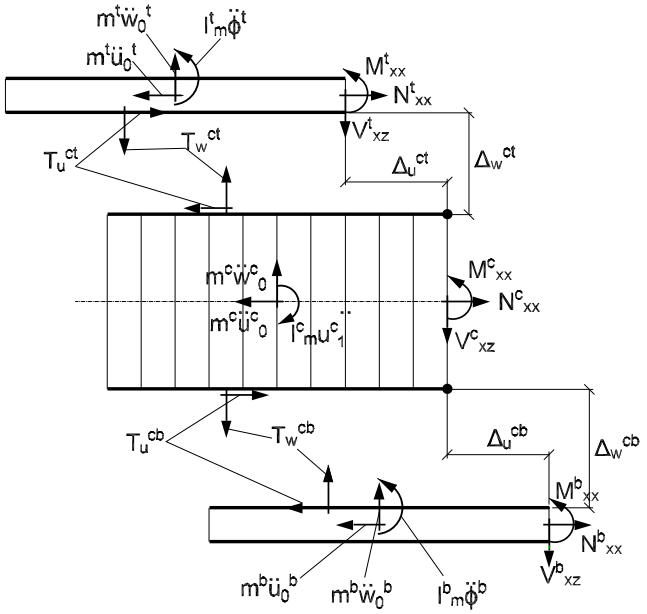

Fig. 2. Traction-Displacement.

2.2. Interfacial traction-displacement gap laws

The respective displacement gaps between the two interfaces, the normal (separation) displacement gap and the tangential (slip) displacement gap between the core to top face sheet (denoted as 'ct') and core to bottom face sheet (denoted as 'cb') are given as,

Core to top face sheet:

$$\Delta_w^{ct} = w_0^c - h^c w_1^c + h^{c^2} w_2^c - w_0^t \tag{7a}$$

$$\Delta_u^{ct} = u_0^c - h^c u_1^c + h^{c^2} u_2^c - h^{c^3} u_3^c - u_0^t + \frac{1}{2} f^t \phi^t \tag{7b}$$

Core to bottom face sheet:

$$\Delta_w^{cb} = w_0^b - w_0^c - h^c w_1^c - h^{c^2} w_2^c \tag{8a}$$

$$\Delta_u^{cb} = u_0^b + \frac{1}{2} f^b \phi^b - u_0^c - h^c u_1^c - h^{c^2} u_2^c - h^{c^3} u_3^c \tag{8b}$$

where, Δ is the differential gap at the respective interfaces. The linear decoupled traction-displacement gap laws are given as,

$$T_w^j(x,t) \;=\; K_w^j \;\Delta_w^j(x,t) \tag{9a}$$

$$T_u^j(x,t) \;=\; K_u^j \;\Delta_u^j(x,t) \tag{9b}$$

where, 'j' = 'ct', 'cb' for the core-top face sheet, core-bottom face sheet interface respectively. K_w^j and K_u^j are the normal and tangential spring stiffness. To simulate disbond the value of K_w^j or K_u^j is taken as zero. Alternatively, to simulate a perfect bond (healthy/pristine panel) a very high value for K_w^j and K_u^j is used to achieve the pseudo-compatibility condition, similar to the penalty method. In addition, these laws can be introduced in the model as a non-linear model [18] reflecting the coupled effect of the slip and separation, describing the nucleation and evolution of the failure mechanism.

2.3. Equations of motion

The governing differential equations (GDEs) are obtained by applying the Hamilton's principle,

$$\delta \int_{t_1}^{t_2} \left(U_e + V_e - T_e \right) \, dt = 0, \tag{10}$$

where, U_e is the strain energy, V_e is the potential energy due to applied loading and T_e is the kinetic energy of the sandwich beam.

The first variation of the strain energy is given as,

$$\begin{aligned} \delta U_e = & \int_{V^t} \left(\sigma_{xx}^t \delta \epsilon_{xx}^t + \tau_{xz}^t \delta \gamma_{xz}^t \right) \, dV^t \; + \int_{V^b} \left(\sigma_{xx}^b \delta \epsilon_{xx}^b + \tau_{xz}^b \delta \gamma_{xz}^b \right) \, dV^b \\ & + \int_{V^c} \left(\sigma_{xx}^c \delta \epsilon_{xx}^c + \sigma_{zz}^c \delta \epsilon_{zz}^c + \tau_{xz}^c \delta \gamma_{xz}^c \right) \, dV^c \\ & + \int_{A^{ct}} \left(T_u^{ct} \delta \Delta_u^{ct} + T_w^{ct} \delta \Delta_w^{ct} \right) \, dA^{ct} \; + \int_{A^{cb}} \left(T_u^{cb} \delta \Delta_u^{cb} + T_w^{cb} \delta \Delta_w^{cb} \right) dA^{cb} \end{aligned} \tag{11a}$$

where, σ_{xx} and ϵ_{xx} are the longitudinal normal stresses and strains respectively, τ_{xz} and γ_{xz} are the transverse shear stress and shear strains respectively, σ_{zz} and ϵ_{zz} are the vertical normal stresses and strains respectively, $dV^i = b \, dx \, dz$ is the infinitesimal volume segment, b is the width of the panel, $dA^j = b \, dx$ is the infinitesimal area segment of each face-core interface (j = 'ct', represents core-top face sheet interface and 'cb', represents core-bottom face sheet interface), T_u and T_w are the

tangential and normal interfacial traction respectively, at the face-core interface, Δ_u and Δ_w are the tangential (sliding) and normal (opening) gaps respectively and superscripts 't', 'b' & 'c' representing the top face sheet, the bottom face sheet and the core respectively.

The first variation of the external loads is given as,

$$\delta V_e = -\int_0^L \left(n^t \delta u_0^t + q^t \delta w_0^t\right)\, dx - \sum_{k=1}^{NC} \int_0^L \left(P_k^t \delta w^t + N_k^t \delta u_0^t + M_k^t \delta \phi^t\right) \delta_D(x - x_k)\, dx \tag{11b}$$

where 'n' represents distributed in-plane force, 'q' the distributed transverse force, 'N_k' the concentrated axial force, 'P_k' the concentrated shear force, 'M_k' the concentrated end moments at $x = x_k$, δ_D is the Dirac delta function, 'NC' is the number of concentrated loads and moments.

The first variation of the kinetic energy is given as,

$$\delta T_e = \int_0^{V^t} \rho^t (\dot{u}^t \delta \dot{u}^t + \dot{w}^t \delta \dot{w}^t)\, dV^t + \int_0^{V^c} \rho^c (\dot{u}^c \delta \dot{u}^c + \dot{w}^c \delta \dot{w}^c)\, dV^c + \int_0^{V^b} \rho^b (\dot{u}^b \delta \dot{u}^b + \dot{w}^b \delta \dot{w}^b)\, dV^b \tag{11c}$$

where, $(\dot{\cdot})$ represents time derivative and 'ρ' denotes the density.

Expressing the stress resultants in the face sheets as,

$$N_{xx}^i = \int_{A^i} \sigma_{xx}^i\, dA^i = b\, A_{11}^i \frac{\partial u_0^i}{\partial x} \tag{12a}$$

$$M_{xx}^i = \int_{A^i} \sigma_{xx}^i\, z^i\, dA^i = -b\, D_{11}^i \frac{\partial \phi^i}{\partial x} \tag{12b}$$

$$V_{xz}^i = \int_{A^i} \tau_{xz}^i\, dA^i = b\, A_{55}^i \left(\frac{\partial w^i}{\partial x} - \phi^i\right) \tag{12c}$$

where, N_{xx}^i, M_{xx}^i and V_{xz}^i (for $i = t$ representing top face sheet, b representing bottom face sheet) are the in-plane, bending moment and shear stress resultants. A_{11}^i, D_{11}^i and A_{55}^i are the extensional, bending and shear stiffness respectively. Expressing the inertia terms as,

$$m^t = \rho^t b f^t,\ I_m^t = \frac{1}{12}\rho^t b f^{t^3},\ \mathrm{m}^b = \rho^b b f^b, I_m^b = \frac{1}{12}\rho^b b f^{b^3},$$
$$m^c = 2\rho^c b h^c,\ I_m^c = \frac{2}{3}\rho^c b h^{c^3},\ J_m^c = \frac{2}{5}\rho^c b h^{c^5}, K_m^c = \frac{2}{7}\rho^c b h^{c^7}, \tag{13}$$

The thirteen governing differential equations (GDEs) of motion obtained are expressed with inertia terms and stress resultants as,

$$\delta u_0^t: \quad -m^t \ddot{u_0}^t + b\, T_u^{ct} + N_{xx,x}^t + n^t = 0 \tag{14a}$$

$$\delta w_0^t: \quad -m^t \ddot{w_0}^t + b\, T_w^{ct} + V_{xz,x}^t + q^t = 0 \tag{14b}$$

$$\delta \phi^t: \quad I_m^t \ddot{\phi}^t + \frac{1}{2} b\, f^t\, T_u^{ct} + M_{xx,x}^t - V_{xz,x}^t = 0 \tag{14c}$$

$$\delta u_0^b: \quad -m^b \ddot{u_0}^b - b\, T_u^{cb} + N_{xx,x}^b = 0 \tag{14d}$$

$$\delta w_0^b: \quad -m^b \ddot{w_0}^b + b\, T_w^{cb} + V_{xz,x}^b = 0 \tag{14e}$$

$$\delta \phi^b: \quad I_m^b \ddot{\phi}^b + \frac{1}{2} b\, f^b\, T_u^{cb} + M_{xx,x}^b - V_{xz,x}^b = 0 \tag{14f}$$

$$\delta u_0^c: \quad -m^c \ddot{u_0}^c - I_m^c \ddot{w_2}^c + b\, T_u^{ct} + b\, T_u^{cb} + N_{xx,x}^c = 0 \tag{14g}$$

$$\delta w_0^c: \quad -m^c \ddot{w_0}^c - I_m^c \ddot{w_2}^c + b\, T_w^{ct} + b\, T_w^{cb} + V_{xz,x}^c = 0 \tag{14h}$$

$$\delta u_1^c: \quad -I_m^c \ddot{u_1}^c - J_m^c \ddot{w_3}^c + b\, h^c\, T_u^{ct} + b\, h^c\, T_u^{cb} + M_{xx,x}^c - V_{xz,x}^c = 0 \tag{14i}$$

$$\delta u_2^c: \quad -I_m^c \ddot{u_0}^c - J_m^c \ddot{w_2}^c - b\, h^{c^2}\, T_u^{ct} + b\, h^{c^2}\, T_u^{cb} + M_{xx2,x}^c - 2\, V_{xz1,x}^c = 0 \tag{14j}$$

$$\delta u_3^c: \quad -J_m^c \ddot{u_1}^c - K_m^c \ddot{w_3}^c + b\, h^{c^3}\, T_u^{ct} + b\, h^{c^3}\, T_u^{cb} + M_{xx3,x}^c - 3\, V_{xz2,x}^c = 0 \tag{14k}$$

$$\delta w_1^c: \quad -I_m^c \ddot{w_1}^c + b\, h^c\, T_w^{ct} + b\, h^c\, T_w^{cb} + V_{xz1,x}^c - R_{zz,x}^c = 0 \tag{14l}$$

$$\delta w_2^c: \quad -I_m^c \ddot{w_0}^c - J_m^c \ddot{w_2}^c - b\, h^{c^2}\, T_w^{ct} + b\, h^{c^2}\, T_w^{cb} + V_{xz2,x}^c - 2\, M_{zz,x}^c = 0 \tag{14m}$$

where, '$f_{,x}$' denotes a derivative of $f(x)$ with respect to x and the stress resultants for the core given as,

$$N_{xx}^c = \int_{A^c} \sigma_{xx}^c dA^c = \frac{b\, E^c}{(1-\nu^{c^2})}\left(\frac{2}{3}h^{c^3}\frac{\partial u_2^c}{\partial x} + 2h^c \frac{\partial u_0^c}{\partial x} + 2\nu^c h^c \frac{\partial w_1^c}{\partial x}\right) \tag{15a}$$

$$M_{xx}^c = \int_{A^c} z^c \sigma_{xx}^c dA^c = \frac{b\, E^c}{(1-\nu^{c^2})}\left(\frac{2}{5}h^{c^5}\frac{\partial u_3^c}{\partial x} + \frac{2}{3}h^{c^3}\frac{\partial u_1^c}{\partial x} + \frac{4}{3}\nu^c h^{c^3}\frac{\partial w_2^c}{\partial x}\right) \tag{15b}$$

$$M_{xx2}^c = \int_{A^c} z^{c^2} \sigma_{xx}^c dA^c = \frac{b\, E^c}{(1-\nu^{c^2})}\left(\frac{2}{5}h^{c^5}\frac{\partial u_2^c}{\partial x} + \frac{2}{3}h^{c^3}\frac{\partial u_0^c}{\partial x} + \frac{2}{3}\nu^c h^{c^3}\frac{\partial w_1^c}{\partial x}\right) \tag{15c}$$

$$M_{xx3}^c = \int_{A^c} z^{c^3} \sigma_{xx}^c dA^c = \frac{b\, E^c}{(1-\nu^{c^2})}\left(\frac{2}{7}h^{c^7}\frac{\partial u_3^c}{\partial x} + \frac{2}{5}h^{c^5}\frac{\partial u_1^c}{\partial x} + \frac{4}{5}\nu^c h^{c^5}\frac{\partial w_2^c}{\partial x}\right) \tag{15d}$$

$$V_{xz}^c = \int_{A^c} \tau_{xz}^c dA^c = b\, G^c\left(2h^{c^3}u_3^c + \frac{2}{3}h^{c^3}\frac{\partial w_2^c}{\partial x} + 2h^c u_1^c + 2h^c \frac{\partial w_0^c}{\partial x}\right) \tag{15e}$$

$$V_{xz1}^c = \int_{A^c} z^c \tau_{xz}^c dA^c = b\, G^c\left(\frac{4}{3}h^{c^3}u_2^c + \frac{2}{3}h^{c^3}\frac{\partial w_1^c}{\partial x}\right) \tag{15f}$$

$$V_{xz2}^c = \int_{A^c} z^{c^2} \tau_{xz}^c dA^c = b\, G^c\left(\frac{6}{5}h^{c^5}u_3^c + \frac{2}{5}h^{c^5}\frac{\partial w_2^c}{\partial x} + \frac{2}{3}h^{c^3}u_1^c + \frac{2}{3}h^{c^3}\frac{\partial w_0^c}{\partial x}\right) \tag{15g}$$

$$R_{zz}^c = \int_{A^c} \sigma_{zz}^c dA^c = \frac{b\, E^c}{(1-\nu^{c^2})}\left(\frac{2}{3}\nu^c h^{c^3}\frac{\partial u_2^c}{\partial x} + 2\nu^c h^c \frac{\partial u_0^c}{\partial x} + 2h^c \frac{\partial w_1^c}{\partial x}\right) \tag{15h}$$

$$M_{zz}^c = z^c \int_{A^c} \sigma_{zz}^c dA^c = \frac{b\, E^c}{(1-\nu^{c^2})}\left(\frac{2}{5}\nu^c h^{c^5}\frac{\partial u_3^c}{\partial x} + \frac{2}{3}\nu^c h^{c^3}\frac{\partial u_1^c}{\partial x} + \frac{4}{3}h^{c^3}\frac{\partial w_2^c}{\partial x}\right) \tag{15i}$$

where, N_{xx}^c, M_{xx}^c and V_{xx}^c are the in-plane, bending moment and shear stress resultants respectively; M_{xx2}^c, M_{xx3}^c, V_{xz1}^c, V_{xz2}^c, R_{zz}^c and M_{zz}^c are the high order mathematical stress resultants.

The thirteen boundary conditions at $x_B = 0$ or L are specified as,

Either:	$u_0^t(x_B) = \bar{\bar{u}}_0^t(x_B)$	or	$\alpha N_{xx}^t(x_B) + N_{x_B}^t = 0$	(16a)
Either:	$w_0^t(x_B) = \bar{\bar{w}}_0^t(x_B)$	or	$\alpha V_{xz}^t(x_B) + P_{x_B}^t = 0$	(16b)
Either:	$\phi^t(x_B) = \bar{\bar{\phi}}^t(x_B)$	or	$\alpha M_{xx}^t(x_B) + M_{x_B}^t = 0$	(16c)
Either:	$u_0^b(x_B) = \bar{\bar{u}}_0^b(x_B)$	or	$\alpha N_{xx}^b(x_B) = 0$	(16d)
Either:	$w_0^b(x_B) = \bar{\bar{w}}_0^t(x_B)$	or	$\alpha V_{xz}^b(x_B) = 0$	(16e)
Either:	$\phi^b(x_B) = \bar{\bar{\phi}}^t(x_B)$	or	$\alpha M_{xx}^b(x_B) = 0$	(16f)
Either:	$u_0^c(x_B) = \bar{\bar{u}}_0^c(x_B)$	or	$\alpha N_{xx}^c(x_B) = 0$	(16g)
Either:	$w_0^c(x_B) = \bar{\bar{w}}_0^c(x_B)$	or	$\alpha V_{xz}^c(x_B) = 0$	(16h)
Either:	$u_1^c(x_B) = \bar{\bar{u}}_1^c(x_B)$	or	$\alpha M_{xx}^c(x_B) = 0$	(16i)
Either:	$u_2^c(x_B) = \bar{\bar{u}}_2^c(x_B)$	or	$\alpha M_{xx2}^c(x_B) = 0$	(16j)
Either:	$u_3^c(x_B) = \bar{\bar{u}}_3^c(x_B)$	or	$\alpha M_{xx3}^c(x_B) = 0$	(16k)

Either: $w_1^c(x_B) = \bar{\bar{w}}_1^c(x_B)$ or $\alpha V_{xz1}^c(x_B) = 0$ (16l)

Either: $w_2^c(x_B) = \bar{\bar{w}}_2^c(x_B)$ or $\alpha V_{xz2}^c(x_B) = 0$ (16m)

where, $\alpha = 1$ for $x_B = 0$ and $\alpha = -1$ for $x_B = L$; $N_{x_B}^t$, $P_{x_B}^t$, $M_{x_B}^t$ are external loads applied on the top face sheet at $x = x_B$ and the double over-bar designate prescribed displacements.

2.4. Solution of the equations of motion

To solve the partial GDEs, the transformation of time dependence is made using the Laplace transform applied to the field variables as,

$$\{\mathbf{U}\} = \mathcal{L}\left\{\begin{array}{l} u_0^t(x,t) \\ w_0^t(x,t) \\ \phi^t(x,t) \\ u_0^b(x,t) \\ w_0^b(x,t) \\ \phi^b(x,t) \\ u_0^c(x,t) \\ w_0^c(x,t) \\ u_1^c(x,t) \\ u_2^c(x,t) \\ u_3^c(x,t) \\ w_1^c(x,t) \\ w_2^c(x,t) \end{array}\right\} = \left\{\begin{array}{l} \bar{u}_0^t(x,s) \\ \bar{\bar{w}}_0^t(x,s) \\ \bar{\phi}^t(x,s) \\ \bar{u}_0^b(x,s) \\ \bar{\bar{w}}_0^b(x,s) \\ \bar{\phi}^b(x,s) \\ \bar{u}_0^c(x,s) \\ \bar{\bar{w}}_0^c(x,s) \\ \bar{u}_1^c(x,s) \\ \bar{u}_2^c(x,s) \\ \bar{u}_3^c(x,s) \\ \bar{\bar{w}}_1^c(x,s) \\ \bar{\bar{w}}_2^c(x,s) \end{array}\right\} \tag{17}$$

where, $s = \sigma + i\,\omega$, 's' is Laplace variable, 'ω' is the angular frequency, 'i' being the imaginary number and $\sigma = \frac{2\pi}{\omega}$ is the real part of the Laplace variable [19]. For example, the GDE Eq. (14a), expressed in terms of displacement function is transformed as,

$$\begin{aligned} &\left(-m^t\, s^2 - b\, K_w^t + b\, A_{11}^t \frac{\partial}{\partial x}\right) \bar{u}_0^t + b\, K_w^t\, \bar{u}_0^c - b\, K_w^t h^c\, \bar{u}_1^c \\ &+ b\, K_w^t\, h^{c^2}\, \bar{u}_2^c - b\, K_w^t\, h^{c^3}\, \bar{u}_3^c + \frac{b\, K_w^t}{2}\, h^c\, \bar{\phi}^t = 0 \end{aligned} \tag{18}$$

All the remaining 12 partial GDEs are thus transformed to ordinary differential equations (ODEs) in terms of 'x' dependence. Thus, the 13 simultaneous ODEs obtained are solved by assuming the solution to be of the form $\bar{u}_0^t(x,s) = \hat{u}_0^t(s)\, e^{-i\,k\,x}$ where, 'k' is the wavenumber and 'i' is the imaginary number. The solutions are assumed similarly to other variables of Eq. (17).

Substituting these in the above GDEs (Eqs. (14a)–(14m)) and expressing them in matrix form results to,

$$[W]_{(13\times 13)}\,\{\hat{\mathbf{U}}\} = 0 \tag{19}$$

where, $\{\hat{\mathbf{U}}\}$ is given as,

$$\begin{aligned} \{\hat{\mathbf{U}}\} = \{&\hat{u}_0^t(s),\ \hat{w}_0^t(s), \hat{\phi}^t(s),\ \hat{u}_0^b(s),\ \hat{w}_0^b(s), \hat{\phi}^b(s), \\ &\hat{u}_0^c(s),\ \hat{w}_0^c(s),\ \hat{u}_1^c(s),\ \hat{u}_2^c(s),\ \hat{u}_3^c(s),\ \hat{w}_1^c(s),\ \hat{w}_2^c(s)\}^T \end{aligned} \tag{20}$$

and $[W]$ is (13 × 13) wave matrix. The elements of each row of $[W]$ are given in Appendix.

The solution to the field variables, $\{\mathbf{U}\}$ are obtained by first expanding the determinant of $[W]$ into polynomial form as,

$$\begin{aligned} &k^{26}\, a_{13} + k^{24}\, a_{12} + k^{22}\, a_{11} + k^{20}\, a_{10} + k^{18}\, a_9 + k^{16}\, a_8 + k^{14}\, a_7 + \\ &k^{12}\, a_6 + k^{10}\, a_5 + k^8\, a_4 + k^6\, a_3 + k^4\, a_2 + k^2\, a_1 + a_0 = 0 \end{aligned} \tag{21}$$

where, the coefficients $a_0 \cdots a_{13}$ are comprised of frequency and material properties. By change of variables say, $r = k^2$, the above equation is solved for the thirteenth order polynomial. In order to compute the roots of this polynomial, it is posed as an eigenvalue problem by forming the companion matrix. The eigenvalues of this matrix are the roots of the polynomial and are computed using the QR algorithm, resulting to 13 roots as r_i, $(i = 1, 2, \ldots, 13)$. The wavenumbers are obtained as $k_i = +\sqrt{r_i}$, $k_j = -\sqrt{r_i}$ where, $i = 1, 2, 3, \ldots, 13$ and $j = 14, 15, 16, \ldots, 26$. Later, using the 26 wavenumbers, the corresponding 26 eigenvectors are obtained from Eq. (19) and are arranged in the amplitude ratio matrix, $\mathbf{R}$ as column vectors. The exact interpolation function is obtained as,

$$\{\mathbf{U}\} = [\mathbf{R}]\,[\Theta]\{\mathbf{a}\} \tag{22}$$

where, $\{\mathbf{a}\}$ is the unknown coefficients vector of size 26 × 1 given as,

$$\begin{aligned} \{\mathbf{a}\} = \{&C_1, C_2, C_3, C_4, C_5, C_6, C_7, C_8, C_9, C_{10}, C_{11}, \\ &C_{12}, C_{13}, C_{14}, C_{15}, C_{16}, C_{17}, C_{18}, C_{19}, C_{20}, C_{21}, \\ &C_{22}, C_{23}, C_{24}, C_{25}, C_{26}\}^T \end{aligned} \tag{23}$$

Θ is a diagonal matrix of size 26 × 26 containing exponential terms,

$$[\Theta]_{[26\times 26]} = \begin{bmatrix} e^{-i\,k_1 x} & 0 & \cdots & \cdots & 0 \\ 0 & e^{-i\,k_2 x} & \cdots & \cdots & 0 \\ \cdot & \cdot & \cdots & \cdots & \cdot \\ \cdot & \cdots & \cdot & \cdots & \cdot \\ \cdot & \cdots & \cdots & e^{-i\,k_{25} x} & \cdot \\ 0 & \cdots & 0 & \cdots & e^{-i\,k_{26} x} \end{bmatrix}$$

and $\mathbf{R}$ is the amplitude ratio matrix of size 13 × 26,

$$[\mathbf{R}]_{[13\times 26]} = \begin{bmatrix} R_{1,1} & R_{1,2} & \cdots & \cdots & R_{1,26} \\ R_{2,1} & R_{2,2} & \cdots & \cdots & R_{2,26} \\ \cdots & \cdots & \cdots & \cdots & \cdots \\ \cdots & \cdots & \cdots & \cdots & \cdots \\ R_{13,1} & R_{13,2} & \cdots & \cdots & R_{13,26} \end{bmatrix}$$

Similarly, the force boundary conditions are transformed using the Laplace transform and the force boundary condition equations (Eqs. (16a)–(16m)) are expressed in matrix form as,

$$\{\hat{\mathbf{f}}\}_{[13\times 1]} = \left[\left(f(k,s)\right)\right]_{[13\times 13]} \left[\mathbf{R}\right]_{[13\times 26]} \left[\Theta\right]_{[26\times 26]} \left\{\mathbf{a}\right\}_{[26\times 1]} \tag{24}$$

Denoting the displacement field vector, $\{\mathbf{U}\}$ and the force vector, $\{\hat{\mathbf{f}}\}$ at node-1 and node-2 with subscripts 1 and 2 the final form of the force–displacement equation is obtained as,

$$\{\hat{\mathbf{u}}\} = \left\{\begin{array}{l} \mathbf{U_{1(x=0)}} \\ \mathbf{U_{2(x=L)}} \end{array}\right\} = [\mathbf{T_1}]\{\mathbf{a}\}$$

$$\left\{\hat{\mathbf{F}}\right\} = \left\{\begin{array}{l} \hat{\mathbf{f}}_{\mathbf{1(x=0)}} \\ -\hat{\mathbf{f}}_{\mathbf{2(x=L)}} \end{array}\right\} = [\mathbf{T_2}]\{\mathbf{a}\}$$

$$\left\{\hat{\mathbf{F}}\right\}_{26\times 1} = [\mathbf{T_2}]\,[\mathbf{T_1}]^{-1}\ \{\hat{\mathbf{u}}\} = [\mathbf{K}]_{26\times 26}\,\{\hat{\mathbf{u}}\}_{26\times 1} \tag{25}$$

where, $[\mathbf{K}]_{26\times 26}$ is the exact dynamic stiffness matrix of the element. From the above equations, the displacement field variables are obtained in the Laplace domain which are transformed back to the spatial-time domain by the inverse transform.

3. Material properties

This section provides the material properties of three different materials that are used here in the examples that follow. The isotropic material considered here is Aluminium and the material properties taken are,

$E_s = 70 \times 10^9$ N/m^2, $\nu = 0.3$, $G_s = \frac{E_s}{2(1+\nu)}$ and $\rho_s = 2800$ kg/m^3,

where, E_s is the elasticity modulus, ν is the Poisson's ratio, G_s is the rigidity modulus and ρ_s is the density of aluminium.

Bi-directional CFRP fabric (43090/M18) is considered for the face sheets of the honeycomb sandwich panels and the tested material properties as given in [20] are,

$E_{11}^{cfrp} = 146.3 \times 10^9$ N/m^2, $G_{13}^{cfrp} = 4.1 \times 10^9$ N/m^2, $\nu^{cfrp} = 0.03$ and $\rho^{cfrp} = 1660$ kg/m^3,

where, the superscript '$cfrp$' denotes the properties of composite face sheets. The honeycomb cells of the core considered here are the regular hexagonal type and the formulae for calculating the material properties

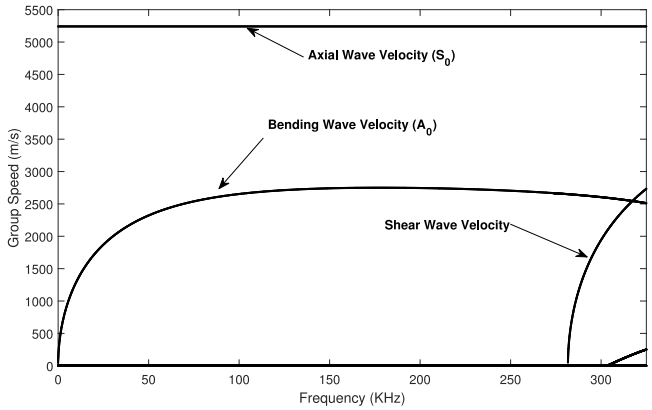

Fig. 3. Group velocity in Aluminium beam.

of the core as presented in [21], is based on the theory that the primary mode of deformation of cellular materials originate from cell wall bending, which agree well with experimental results.

$Density of the core,\ \rho^c = \rho_s \left(\frac{2}{\sqrt{3}}\right)\left(\frac{t_w}{l_w}\right)$,

$Young's modulus,\ E_{11}^c = 2.3\left(\frac{t_w}{l_w}\right)^3 E_s, E_{33}^c = \left(\frac{t_w}{l_w}\right) E_s$,

$Rigidity Modulus,\ G_{13}^c = 0.577\left(\frac{t_w}{l_w}\right) G_s$,

$Poisson's ratio,\ \nu_{13}^c = \frac{E_{11}}{E_{33}}\nu_s$.

where subscript 's' indicates the base material. Here, considering the Aluminium regular hexagonal core with cell wall thickness $t_w = 0.0178 \times 10^{-3}$ m and cell size 4.763×10^{-3} m, the material properties are obtained as,

$E_{11}^c = 4.0313{\times}10^4$ N/m^2, $E_{33}^c = 5.2054{\times}10^8$ N/m^2, $G_{13}^c = 1.00{\times}10^8$ N/m^2, $\nu^c = 2.67 \times 10^{-5} \approx 0.0$ and $\rho^c = 20.91$ kg/m^3. where, the superscript 'c' denotes the properties of core.

4. Wave propagation characteristics

Wave propagation characteristics are studied using the spectrum and dispersion relations which are necessary to determine the nature of waves propagating in a medium. In the spectrum relation the wavenumbers are plotted against the frequency and in the dispersion relation the phase speed and group speed are plotted for various frequencies, which are presented in this section for both isotropic case and sandwich case.

The wavenumbers are obtained by solving Eq. (21) for 'k' and similarly, the group speed $c_g = \frac{\partial\omega}{\partial k}$ as well as phase speed $c_p = \frac{\omega}{k}$ are obtained using equation Eq. (21).

4.1. Isotropic case

To study the dispersion characteristics in an isotropic material, an Aluminium beam with the cross-sectional geometric properties taken as, width, $b = 50{\times}10^{-3}$ m and height, $h = 5{\times}10^{-3}$ m, is considered in this example. A shear correction factor, $k_c = \frac{5}{6}$ is introduced in computing the group velocity. The group velocity plot is shown in Fig. 3.

The plot shows the non-dispersive axial wave with a velocity of 5241.4 m/s and the bending wave velocity following the profile as given in Ref. [7]. In addition, the velocity profile of the shear wave that usually occurs in thick beams, is plotted in the figure. The cut-off frequency for the shear wave derived in [7] is given as, $f_{cut-off} = \frac{1}{2\pi}\sqrt{\frac{G\,A\,\pi^2}{12\,\rho\,I_0}}$ where, A is the cross-sectional area and $I_0 = \frac{b\,h^3}{12}$ is the cross-sectional inertia. The value of the cut-off frequency obtained from the plot is $\approx$ 282 kHz which matches with the given formula. This example primarily serves to validate the formulated element as regard to the wave propagation characteristics.

4.2. Honeycomb sandwich

A honeycomb sandwich panel composed that of $\left[0_2^\circ/90_2^\circ\right]$ cross-ply graphite-epoxy composite laminate for top and bottom face sheets with Aluminium honeycomb core, is considered in this example. The material properties are as given in the 'Material properties' section. The geometrical properties of the sandwich panel cross-section are, $f^t = f^b = 0.16 \times 10^{-3}$ m and $2\,h^c = 15 \times 10^{-3}$ m where, f^t, f^b and $2\,h^c$ are the thickness of the top face sheet, bottom face sheet and core.

Fig. 4(a) and Fig. 4(b) shows the spectrum plots where the real part of the wavenumber is plotted against frequency and the imaginary component of the wavenumber is plotted against frequency respectively. The non-dimensional real part of the wavenumber represents the propagating waves while the non-dimensional imaginary part of the wavenumber represents evanescent waves. As the primary motivation is damage identification, here only the fundamental symmetric S_0 mode and anti-symmetric A_0 mode are specifically indicated. The other modes can be identified as detailed in [13], by exciting particular degrees of freedom (DOF) and identifying the dominant response based on the time of arrival using the group velocity plot.

The dispersion plots are obtained by plotting the group velocity, $c_g = \frac{\partial\omega}{\partial k}$ with respect to frequency and phase speed, $c_p = \frac{\omega}{k}$ with respect to frequency as shown in Fig. 4(c) and Fig. 4(d) respectively, where 'ω' is the angular frequency and 'k' is the wavenumber. In Fig. 4(c) it can be seen the axial wave mode (S_0) is also dispersive, unlike the isotropic case (Fig. 3). At low frequency the bending wave is dispersive and at very high frequencies it becomes non-dispersive reaching the Rayleigh-like surface wave speeds. This can also be observed in phase speed plot (Fig. 4(d)), where the S_0 and A_0 mode reach same speeds at high frequencies. At particular frequency around 67 kHz it can be seen that S_0 mode becomes non-propagating. In addition, it can be seen in phase speed plot, large velocity change (starting from infinity) for higher order modes at the same frequencies. At these frequencies, the group velocities being zero indicate standing waves. In the group speed plot (Fig. 4(c)), particularly at around 77 kHz, negative group velocity is seen when the phase speeds are positive, suggesting that the energy transport is in the opposite direction of the wave speed. These phenomena are reported in literature as backward wave propagation in [22] and in others as negative group velocities [23,24].

The dispersion plot of a disbonded panel with top face sheet–core disbond is super imposed on the dispersion plot of a healthy (pristine) sandwich panel and is shown in Fig. 5. The thick solid lines represents the spectrum of the disbonded panel and the thin lines are that of the healthy panel.

Here, first it can be observed the $S_0^{DISBOND}$ mode is non-dispersive as the top face sheet is disbonded from the core and acts as a thin beam resulting in the axial velocity in the CFRP face sheet. Similarly, the $A_0^{DISBOND}$ mode of the disbonded top face sheet, shown in Fig. 5, follows the profile of that of a thin beam as given in [8]. The S_0^* and A_0^* gives the axial and transverse velocities of the bottom face sheet perfectly bonded to the core and are both dispersive. It is to be noted that due to the asymmetry of the waveguide, standard classification into symmetric and anti-symmetric waves is not possible and S_0^*, A_0^* are only used as notations for referring to those modes. Secondly, in the lower frequency range (up-to 60 kHz) the bending wave mode shows higher velocities in the disbonded panel (A_0^*) as compared to the healthy panel (A_0) and at higher frequencies both arrive at the same velocities, reaching surface wave speeds. Finally, the S_0 shown in the figure gives the axial wave velocity and A_0 the transverse wave velocity in a perfectly bonded healthy panel.

5. Validation with finite element results

Here, the performance of the developed spectral finite element is validated by comparing the responses obtained by the finite element method (FEM); first for isotropic beam and later for honeycomb sandwich panel.

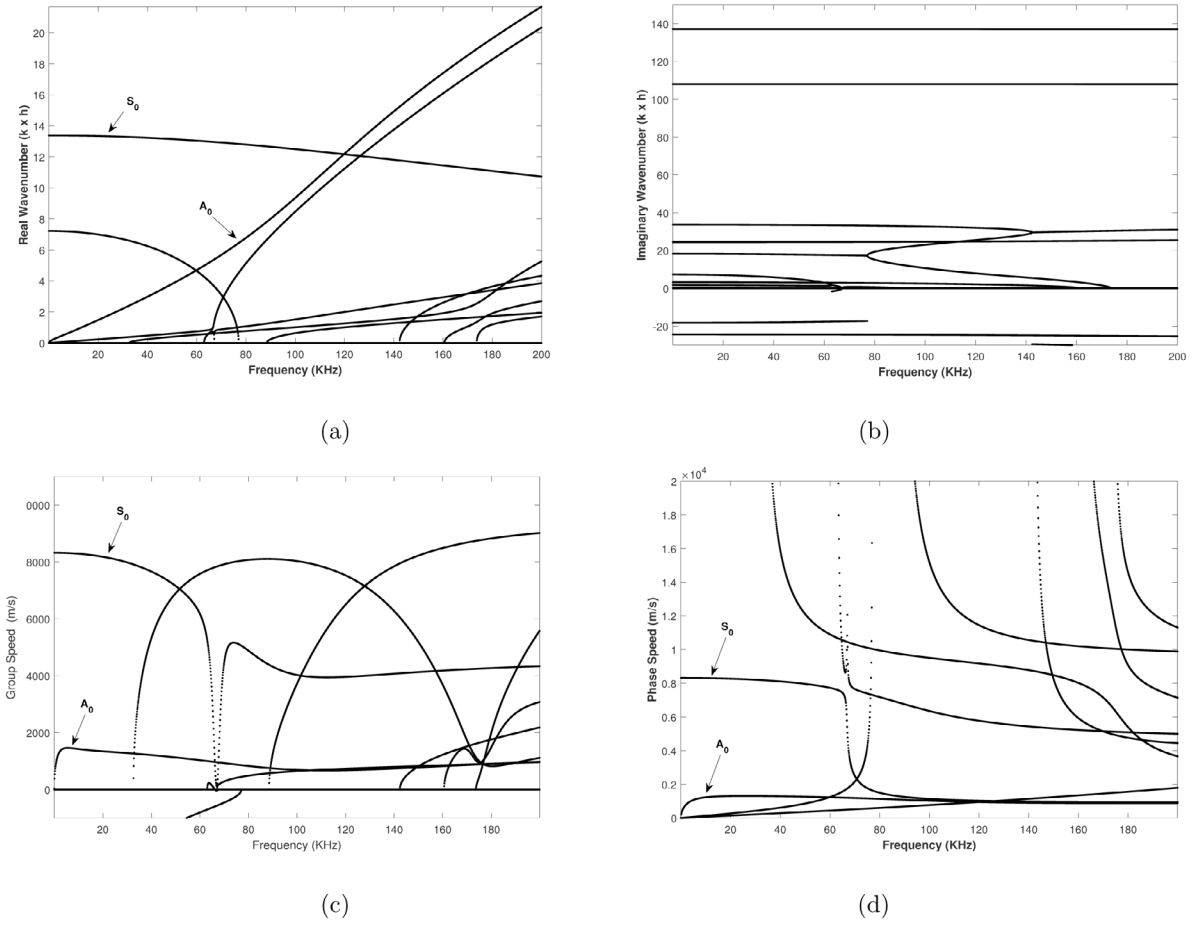

Fig. 4. (a) Real part of wavenumber, (b) Imaginary part of wavenumber, (c) Group velocity (m/s), (d) Phase speed (m/s).

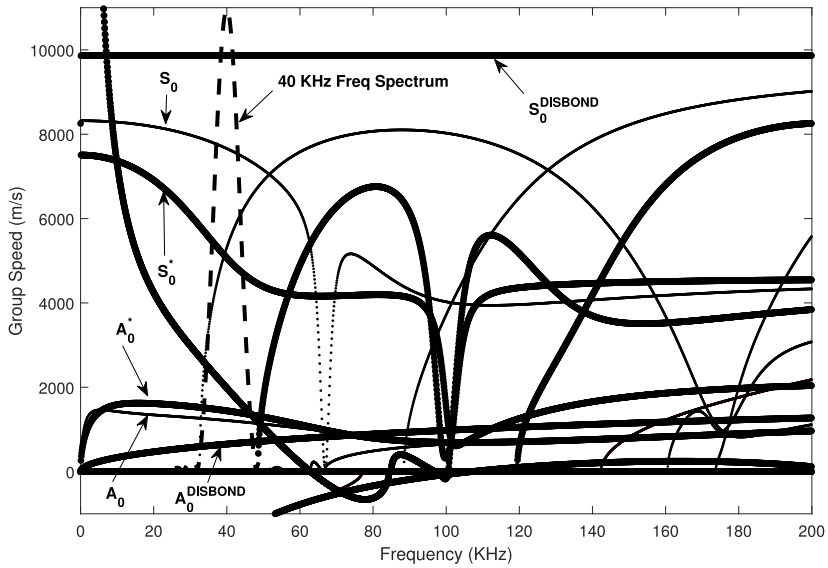

Fig. 5. Superimposed group velocities of disbond and healthy sandwich panel.

5.1. Isotropic Aluminium beam

A cantilever beam is considered with the following geometrical properties, Length, $L = 500\times10^{-3}$ m, width, $b = 50\times10^{-3}$ m and height of the beam, $h = 5\times10^{-3}$ m. The material properties are as given in the 'Material properties' section. First, a finite element model is built using MSC Nastran CBAR elements. To obtain a converged solution, the beam is modelled with a refined finite element mesh resulting to around 1000 DOFs. The beam is fixed at one end while the other end is free. In the spectral finite element method (SFEM) only one spectral finite element is used to model the beam. To have a perfect bond between layers, the values for spring stiffness given in the traction laws are arrived as, $K_u = \alpha_u \times 10^6$ (N/m) and $K_w = \alpha_w \times 10^6$ (N/m) where, $\alpha_u = A_{11}$

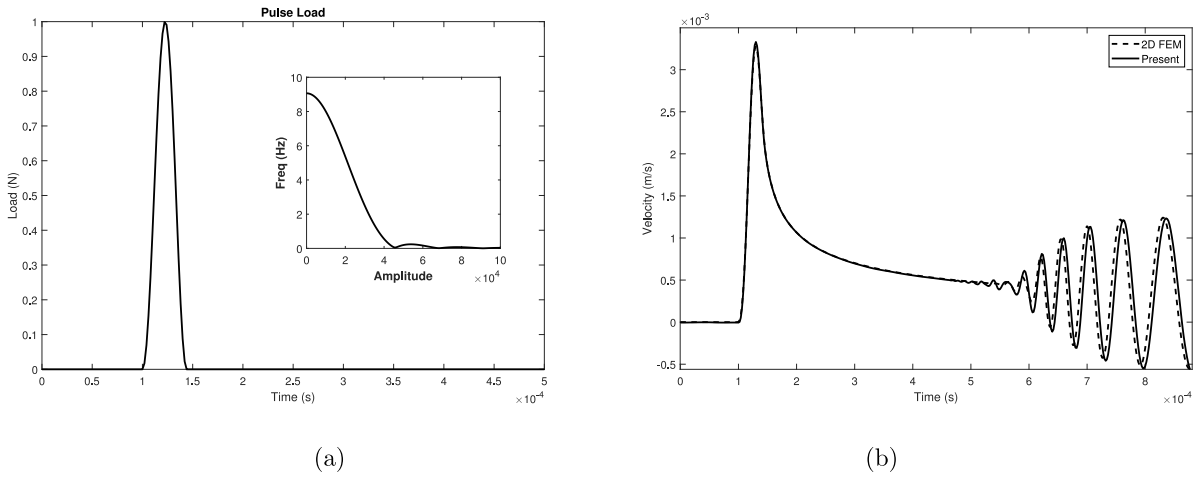

Fig. 6. (a) Pulse load, (b) Transverse velocity for isotropic beam (m/s).

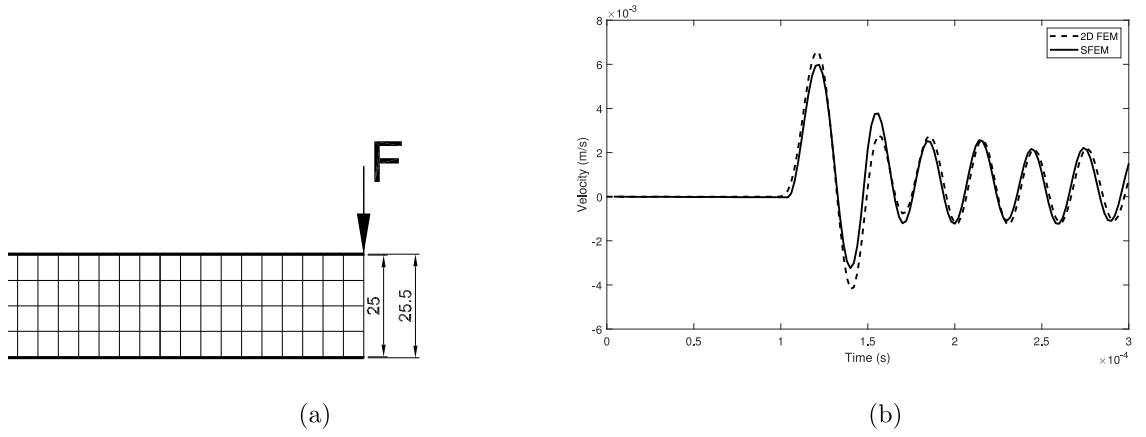

Fig. 7. (a) Finite Element Model, (b) Transverse velocity for sandwich panel (m/s).

and $\alpha_w = D_{11}$. These stiffness values are found sufficient to enforce the penalty conditions. A broad-band pulse as shown in Fig. 6(a) is applied at the free end and the velocity response obtained at the free end is plotted in Fig. 6(b). The plot shows the responses obtained by both SFEM and FEM match perfectly.

5.2. Honeycomb sandwich panel

Honeycomb sandwich panel with aluminium face sheets and aluminium core is considered here with the following geometrical properties, Length, $L = 500 \times 10^{-3}$ m, width, $b = 200 \times 10^{-3}$ m, $f^t = f^b = 0.25 \times 10^{-3}$ m and $2h^c = 25 \times 10^{-3}$ m. The cantilever beam is fixed at one end and a pulse load (Fig. 6(a)) is applied on the tip of the top face sheet at the free end. The response is obtained at the same location.

Here, in the finite element (FE) model, MSC Nastran CQUAD4 elements are used to model for both face sheets and the core. To have a converged solution, the beam is modelled with a refined finite element mesh resulting to around 3000 DOFs. In the SFEM, the same configuration is modelled with only one spectral finite element. Similar to that given in the isotropic case, to have a perfect bond between layers, the values for the spring stiffness are taken as, $K_u = \alpha_u \times 10^6$ (N/m) and $K_w = \alpha_w \times 10^6$ (N/m) where, $\alpha_u = A^i_{11}$ and $\alpha_w = D^i_{11}$ and A_{11}, D_{11} are stiffness coefficients, 'i' = 't' for top face sheet and 'i' = 'b' for bottom face sheet. The FE model is shown in Fig. 7(a) and the velocity response obtained by the FEM and the SFEM is shown in Fig. 7(b). The responses obtained from both the methods match well, thus validating the developed spectral element. This example shows that using the developed spectral element, one can obtain the response without the use of large-sized finite element model.

These examples not only validate the developed spectral finite element, but also gives an estimate for the spring stiffness that is to be used to enforce the penalty constraints for a healthy panel.

5.3. Response in disbonded honeycomb sandwich panel

The same cantilever honeycomb panel as given in the previous section is considered, but by introducing a face sheet–core disbond of length $L_{DISBOND} = 50 \times 10^{-3}$ m at a distance of 200×10^{-3} m from the fixed end. To simulate the disbond between the top face sheet and core the stiffness value $K^t_w = 0.0$ N/m is introduced in the disbond region of the spectral finite element model. In the finite element model the nodes between the face sheet and core for the length of disbond are free and are not merged. Fig. 8(a) shows the cantilever beam with 'F' indicating a 44 kHz pulse load as shown in Fig. 6(a), applied at the free end of the cantilever. All dimensions shown in Fig. 8(a) are in mm. The acceleration response is measured at the tip and is shown Fig. 8(b). The acceleration response obtained by the SFEM and that obtained with FEM shows a good match.

6. Studies on disbond between face sheet and core

In this section, a tone burst signal is used to first estimate the damping of the core and later the same signal is used to inspect the face sheet disbond in a sandwich panel. In all the examples in this

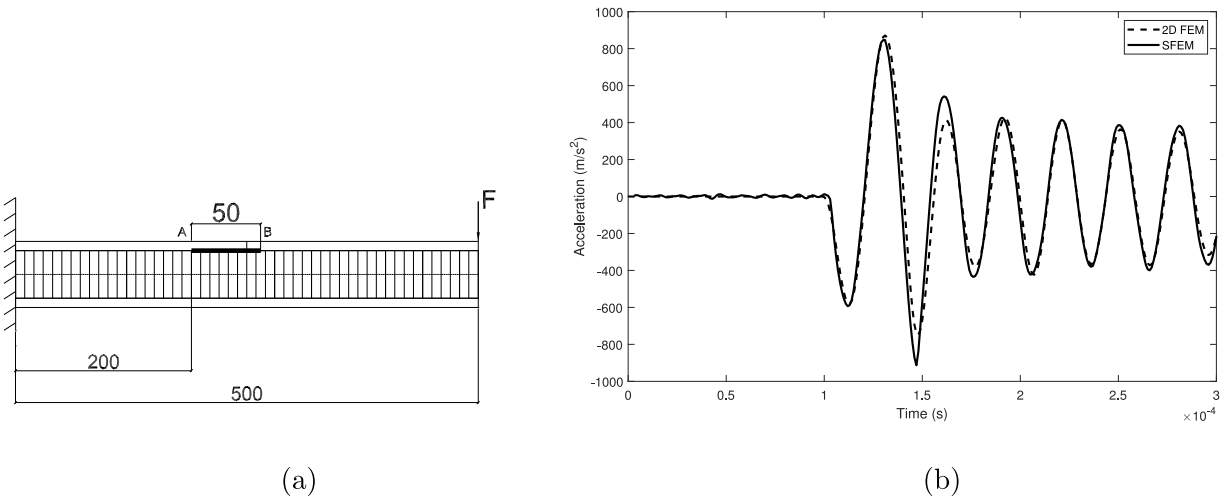

Fig. 8. (a) Cantilever with disbond, (b) Acceleration response at the tip (m/s^2).

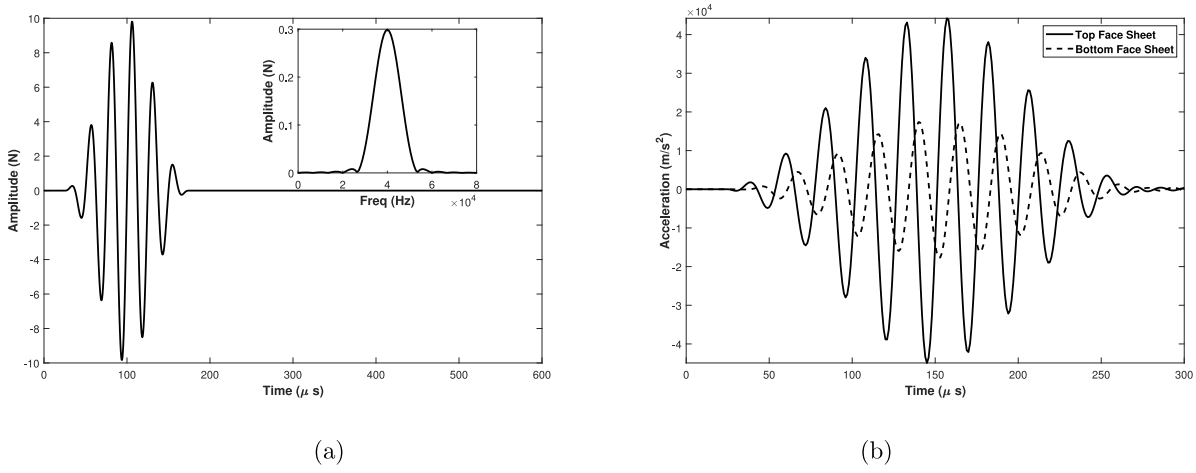

Fig. 9. (a) 40 KHz Tone burst, (b) Core damping effect.

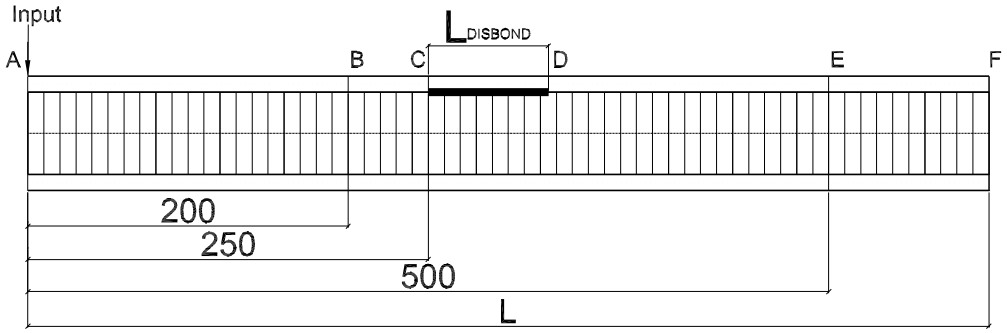

Fig. 10. Face sheet core disbond sandwich panel.

section, a honeycomb sandwich panel with bi-directional CFRP fabric (43090/M18) face sheets and aluminium honeycomb core is considered with $f^t = f^b = 0.16 \times 10^{-3}$ m and $2h^c = 15 \times 10^{-3}$ m, where, f^t, f^b and $2h^c$ are the thickness of the top face sheet, bottom face sheet and core.

6.1. Core damping

Here, the natural damping effect of the core is demonstrated. Fig. 9(a) shows a 40 kHz tone burst signal that is used to excite an un-damped sandwich panel at a point on the top face sheet and the responses are measured at the same point on both the top face sheet and the bottom face sheet. The responses of both top face sheet and bottom face sheet are shown in Fig. 9(b). The plot shows time delay (≈7 μs) between the peaks of the top face sheet response and the bottom face sheet response. In addition, the plot very clearly shows the amplitude reduction between the bottom face sheet response and the top face sheet response. This amplitude reduction is the effect of core damping which contributes substantially to the distortion and decay of the propagating waves. Though this example shows through-thickness damping of the core, the damping can also be observed in the propagating direction as presented in the disbond sub-section,

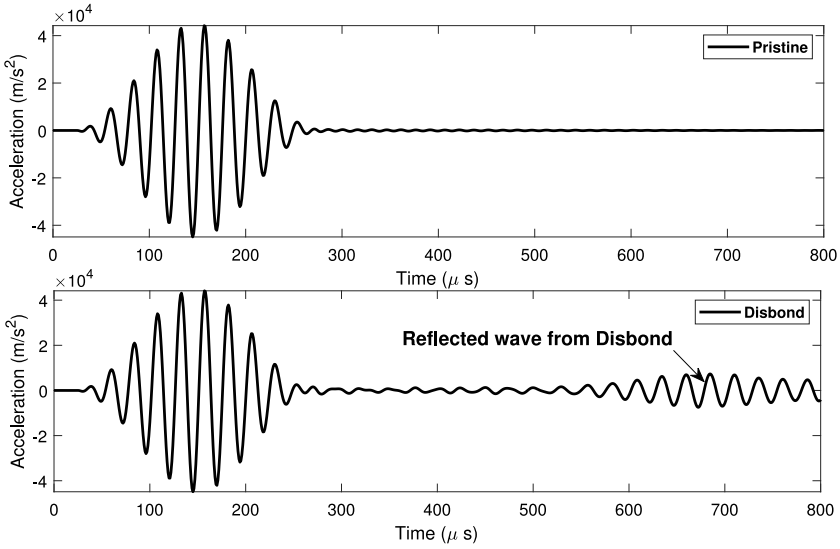

Fig. 11. Response measured at input point, '*A*'.

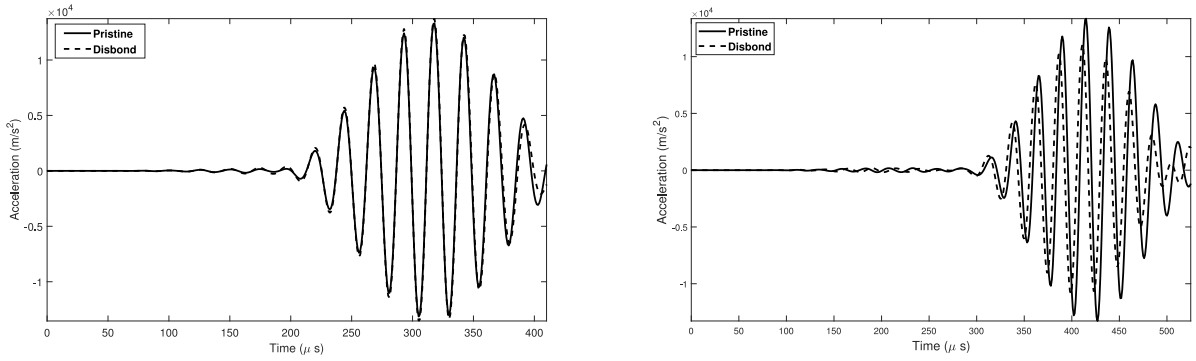

(a) At point '*B*' (b) On disbond

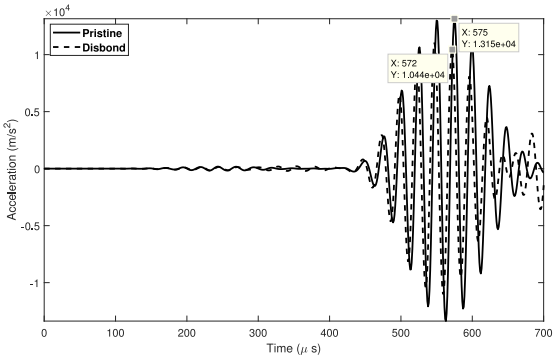

(c) At point '*E*'

Fig. 12. Disbond length $L_{DISBOND} = 50$ mm.

where the wave is attenuated for travelling a distance of 200×10^{-3} m. Compared to the input in the top plot of Fig. 11, it can be seen there is an amplitude reduction in the response plot of Fig. 12. This study suggests that the core acts as a damping medium and further detailed design studies can be made to utilize this core behaviour to safeguard sensitive equipment from vibrations that would be mounted on the other side of the panel.

6.2. Face sheet–core disbond

Here, a disbond between top face sheet and the core is considered. The stiffness $K_w^t = 0.0$ N/m, is used to simulate the disbond in the disbonded spectral finite elements. The sandwich panel with top face sheet–core disbond is depicted in Fig. 10 where, all dimensions shown in the figure are in mm. A 40 kHz tone burst signal as shown in Fig. 9(a) is used as an input to excite the beam transversely and only propagating

waves are considered. The frequency content of this tone burst load is indicated with a dashed line in the dispersion plot of Fig. 5.

The total length of the beam, $L = 1.5$ m with a disbond length denoted as $L_{DISBOND}$, is considered. The panel is modelled with healthy elements ($A-B$, $B-C$, $D-E\&E-F$) and disbond elements ($C-D$) along with a throw-off element at the end 'F', to damp out the reflections from that end.

As a preliminary example, to inspect the presence of disbond, the panel is excited at point 'A' and the response is measured at point 'A'. Here, the choice of the loading frequency can be made with the help of Fig. 5. In Fig. 5, a dashed line depicting '40 kHz Freq Spectrum' is shown. This 40 kHz frequency is chosen as the group velocities of A_0 and A_0^* modes of healthy and disbonded panel respectively show difference in that region. Second, choosing higher frequency in that region results in shorter wavelength and helps in identifying small-sized defects. The top plot in Fig. 11 shows the measured signal in a healthy panel, for the 40 kHz input signal which forms the baseline signal. The bottom plot gives the measured response for the disbonded panel, where the reflection from the disbond can be observed. The reflection from the disbond is captured and the time of arrival is measured. The velocity of the reflected wave is thus computed and is found to match with the velocity obtained from the group velocity plot (Fig. 5).

Due to a disbond between one of the CFRP skins and the honeycomb core of a sandwich panel, the skin will function as a separate waveguide for guided waves. This effect is studied further by studying the propagating behaviour of the tone burst signal along the length of the sandwich panel by considering both healthy panel and disbonded panel. In the disbonded panel, the length of the disbond considered is $L_{DISBOND} = 50\times10^{-3}$ m.

The beam is excited at point 'A' and Fig. 12(a) shows responses measured at point 'B', which is 50×10^{-3} m before the disbond. It can be seen that the response for both healthy/pristine panel and the disbond panel match perfectly. There is no lead/lag time between the responses and no difference in amplitude can be seen.

Fig. 12(b) shows responses measured on the disbond. Here, it can be observed that the tone burst signal arrives before in the disbond panel as compared to the arrival time in the healthy panel. This is in accordance to the group velocity plot shown in Fig. 5. In addition, the disbonded panel response shows amplitude reduction as compared with the healthy panel response.

Fig. 12(c) shows responses measured at point 'E', which is 500×10^{-3} m from the point of excitation and is far away from the disbond. Here, again it can be observed that the response to the input signal in the disbonded panel arrives before and there is an amplitude reduction. The time interval between the two signals is found to be 3 μs. Comparing Fig. 12(b) and (c), it can be seen that except for the amplitude change there is no significant lead/lag time between healthy and disbonded panel. The disbond length being small, the stiffness of the disbonded structure is not altered much.

To investigate further, a study was conducted by considering a disbond length $L_{DISBOND} = 100\times10^{-3}$ m and the responses are measured at the same locations as given in the previous case. Fig. 13(a) shows response at point 'B' (before the disbond), Fig. 13(b) shows the response plot at a location on the disbond and Fig. 13(c) shows the response plot at 'E' (after the disbond).

Similar to the earlier case, responses obtained from both healthy and disbonded panel match perfectly at point 'B', before the disbond. But the responses on the disbond differs from the previous case. First, there is a significant delay in the disbond panel response as compared with the healthy panel response by about 39 μs. This can be attributed to the reduced stiffness, leading to lower propagating velocity. This is because in the disbond region, the waves are travelling in the face sheet alone and the velocity is given by $A_0^{DISBOND}$ mode as shown in Fig. 5. Second, the wave amplitude is higher in the disbonded panel response than in the healthy panel response. This is because the disbonded face sheet, in this case, due to its increased length of disbond (100×10^{-3}) is more pliable as compared to that with shorter disbond length with increased stiffness, in the previous case having disbond length of 50×10^{-3} m.

Finally, Fig. 13(c) reveals a similar trend as seen in the previous example (Fig. 12(c)). But here the lead time is 6 μs as compared with 3 μs in the previous example. This difference can be attributed to the disbond length which is double the size of disbond considered in the previous example. This lead time (i.e., the arrival of the wave in a disbonded panel before that of the healthy panel) is also observed through laboratory experiments in [25].

Thus, from these examples, it can be stated that amplitude change (amplification/reduction) is a measure to identify the disbond and the lead/lag time can be used to arrive at the length of disbond. Thus, these cases can be used to recognize by an automated damage detection algorithm needed for NDE applications.

7. Conclusion

Spectral finite element for a sandwich panel with compressible core is formulated, to address the core–face sheet disbond by incorporating interfacial traction-displacement gap laws between the face sheet and the core interface. It is shown that the same element can be used for a healthy specimen. In validating the responses obtained through the spectral finite element method with that obtained by the finite element method for both isotropic cases as well as honeycomb sandwich cases, the spring stiffness required for a healthy element is obtained. Studies on the wave propagation characteristics in both healthy panel and disbonded panel is presented, suggesting in making a choice for the frequency content of a tone burst signal. Later, detailed numerical studies on the core–face sheet disbond were conducted and is shown that the response amplitude identifies a disbond whereas the arrival time of the wave can be used to size the disbond. Numerical examples show that with the formulated spectral finite element, the detection of a hidden core–face sheet disbond in complex anisotropic structural components can be simulated efficiently using high frequency ultrasonic guided waves.

CRediT authorship contribution statement

M.V.V.S. Murthy: Conception and design of study, Analysis and/or interpretation of data, Writing - original draft. **S. Gopalakrishnan:** Conception and design of study, Analysis and/or interpretation of data, Writing – review & editing. **D. Poomani:** Conception and design of study, Writing – original draft, Writing – review & editing.

Acknowledgment

Approval of the version of the manuscript to be published (the names of all authors must be listed): M. V. V. S. Murthy. S. Gopalakrishanan. D. Poomani.

Declaration of competing interest

The authors declare that they have no known competing financial interests or personal relationships that could have appeared to influence the work reported in this paper.

Appendix

The elements of each row of the wave matrix $[W]_{(13\times13)}$ in Eq. (19) are given as,

1st row of [W]

$W(1,1) = -A_{11}^t\ b\ k^2 - m^t\ s^2 - K_u^t\ b,$

$W(1,2) = 0,$

$W(1,3) = (K_u^t\ b\ f^t)/2,$

$W(1,4) = 0,$

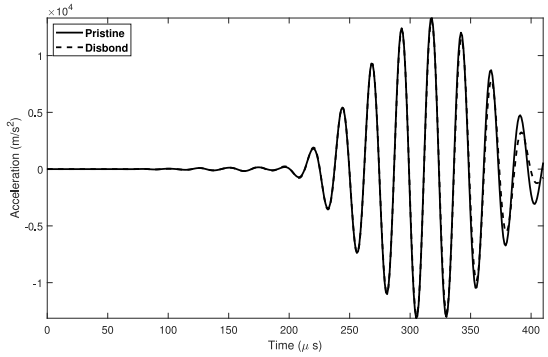

(a) At point 'B'

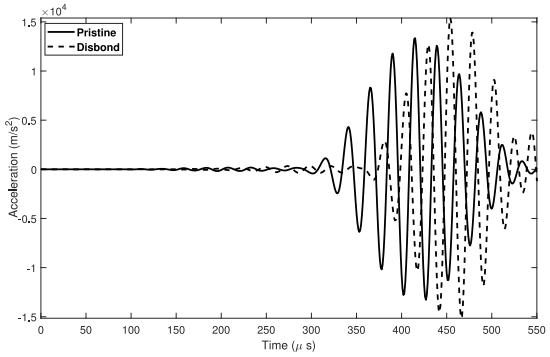

(b) On disbond

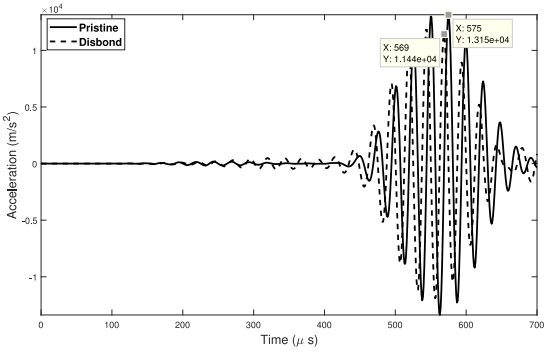

(c) At point 'E'

Fig. 13. Response for disbond length $L_{DISBOND} = 100$ mm.

$W(1,5) = 0,$
$W(1,6) = 0,$
$W(1,7) = K_u^t\ b,$
$W(1,8) = 0,$
$W(1,9) = -K_u^t\ b\ h^c,$
$W(1,10) = K_u^t\ b\ h^{c^2},$
$W(1,11) = -K_u^t\ b\ h^{c^3},$
$W(1,12) = 0,$
$W(1,13) = 0.$

2nd row of [W]

$W(2,1) = 0,$
$W(2,2) = -A_{55}^t\ b\ k^2 - m^t\ s^2 - K_w^t\ b,$
$W(2,3) = A_{55}^t\ b\ i\ k,$
$W(2,4) = 0,$
$W(2,5) = 0,$
$W(2,6) = 0,$
$W(2,7) = 0,$
$W(2,8) = K_w^t\ b,$
$W(2,9) = 0,$
$W(2,10) = 0,$
$W(2,11) = 0,$
$W(2,12) = -K_w^t\ b\ h^c,$
$W(2,13) = K_w^t\ b\ h^{c^2}.$

3rd row of [W]

$W(3,1) = -(K_u^t\ b\ f^t)/2,$
$W(3,2) = A_{55}^t\ b\ i\ k,$
$W(3,3) = (K_u^t\ b\ f^{t^2})/4 + D_{11}^t\ b\ k^2 + I_m^t\ s^2 + A_{55}^t\ b,$
$W(3,4) = 0,$
$W(3,5) = 0,$
$W(3,6) = 0,$
$W(3,7) = (K_u^t\ b\ f^t)/2,$
$W(3,8) = 0,$
$W(3,9) = -(K_u^t\ b\ f^t\ h^c)/2,$
$W(3,10) = (K_u^t\ b\ f^t\ h^{c^2})/2,$
$W(3,11) = -(K_u^t\ b\ f^t\ h^{c^3})/2,$
$W(3,12) = 0,$
$W(3,13) = 0.$

4th row of [W]

$W(4,1) = 0,$
$W(4,2) = 0,$
$W(4,3) = 0,$
$W(4,4) = -A_{11}^b\ b\ k^2 - m^b\ s^2 - K_u^b\ b,$
$W(4,5) = 0,$
$W(4,6) = -(K_u^b\ b\ f^b)/2,$
$W(4,7) = K_u^b\ b,$
$W(4,8) = 0,$
$W(4,9) = K_u^b\ b\ h^c,$
$W(4,10) = K_u^b\ b\ h^{c^2},$
$W(4,11) = K_u^b\ b\ h^{c^3},$
$W(4,12) = 0,$
$W(4,13) = 0.$

5th row of [W]

$W(5,1) = 0,$
$W(5,2) = 0,$
$W(5,3) = 0,$
$W(5,4) = 0,$
$W(5,5) = -A_{55}^b\ b\ k^2 - m^b\ s^2 - K_w^b\ b,$
$W(5,6) = A_{55}^b\ b\ i\ k,$
$W(5,7) = 0,$
$W(5,8) = K_w^b\ b,$

$W(5,9) = 0,$
$W(5,10) = 0,$
$W(5,11) = 0,$
$W(5,12) = K_w^b\ b\ h^c,$
$W(5,13) = K_w^b\ b\ h^{c^2}$

6th row of [W]

$W(6,1) = 0,$
$W(6,2) = 0,$
$W(6,3) = 0,$
$W(6,4) = (K_u^b\ b\ f^b)/2,$
$W(6,5) = A_{55}^b\ b\ i\ k,$
$W(6,6) = (K_u^b\ b\ f^{b^2})/4 + D_{11} b\ b\ k^2 + I_m^b\ s^2 + A_{55}^b\ b,$
$W(6,7) = -(K_u^b\ b\ f^b)/2,$
$W(6,8) = 0,$
$W(6,9) = -(K_u^b\ b\ f^b\ h^c)/2,$
$W(6,10) = -(K_u^b\ b\ f^b\ h^{c^2})/2,$
$W(6,11) = -(K_u^b\ b\ f^b\ h^{c^3})/2,$
$W(6,12) = 0,$
$W(6,13) = 0.$

7th row of [W]

$W(7,1) = K_u^t\ b,$
$W(7,2) = 0,$
$W(7,3) = -(K_u^t\ b\ f^t)/2,$
$W(7,4) = K_u^b\ b,$
$W(7,5) = 0,$
$W(7,6) = (K_u^b\ b\ f^b)/2,$
$W(7,7) = (2\ E^c\ b\ h^c\ k^2)/(\nu^{c^2} - 1) - K_u^t\ b - m^c\ s^2 - K_u^b\ b,$
$W(7,8) = (2\ E^c\ b\ i\ h^c\ k\ \nu^c)/(\nu^{c^2} - 1),$
$W(7,9) = K_u^t\ b\ h^c - K_u^b\ b\ h^c,$
$W(7,10) = (2\ E^c\ b\ h^{c^3}\ k^2)/(3\ \nu^{c^2} - 3) - K_u^b\ b\ h^{c^2} - K_u^t\ b\ h^{c^2} - I_m^c\ s^2,$
$W(7,11) = K_u^t\ b\ h^{c^3} - K_u^b\ b\ h^{c^3},$
$W(7,12) = 0,$
$W(7,13) = 0.$

8th row of [W]

$W(8,1) = 0,$
$W(8,2) = K_w^t\ b,$
$W(8,3) = 0,$
$W(8,4) = 0,$
$W(8,5) = K_w^b\ b,$
$W(8,6) = 0,$
$W(8,7) = 0,$
$W(8,8) = -2\ G^c\ b\ h^c\ k^2 - m^c\ s^2 - K_w^b\ b - K_w^t\ b,$
$W(8,9) = -2\ G^c\ b\ i\ h^c\ k,$
$W(8,10) = 0,$
$W(8,11) = -2\ G^c\ b\ i\ h^{c^3}\ k,$
$W(8,12) = K_w^t\ b\ h^c - K_w^b\ b\ h^c,$
$W(8,13) = -I_m^c\ s^2 - K_w^b\ b\ h^{c^2} - K_w^t\ b\ h^{c^2} - (2\ G^c\ b\ h^{c^3}\ k^2)/3.$

9th row of [W]

$W(9,1) = -K_u^t\ b\ h^c,$
$W(9,2) = 0,$
$W(9,3) = (K_u^t\ b\ f^t\ h^c)/2,$
$W(9,4) = K_u^b\ b\ h^c,$
$W(9,5) = 0,$
$W(9,6) = (K_u^b\ b\ f^b\ h^c)/2,$
$W(9,7) = K_u^t\ b\ h^c - K_u^b\ b\ h^c,$
$W(9,8) = 2\ G^c\ b\ i\ h^c\ k,$
$W(9,9) = (2\ E^c\ b\ h^{c^3}\ k^2)/(3\ \nu^{c^2} - 3) - 2\ G^c\ b\ h^c - K_u^b\ b\ h^{c^2} - K_u^t\ b\ h^{c^2} - I_m^c\ s^2,$
$W(9,10) = K_u^t\ b\ h^{c^3} - K_u^b\ b\ h^{c^3},$
$W(9,11) = (2\ E^c\ b\ h^{c^5}\ k^2)/(5\ \nu^{c^2} - 5) - 2\ G^c\ b\ h^{c^3} - K_u^b\ b\ h^{c^4} - K_u^t\ b\ h^{c^4} - J_m^c\ s^2,$
$W(9,12) = 0,$
$W(9,13) = (2\ G^c\ b\ i\ h^{c^3}\ k)/3 + (4\ E^c\ b\ i\ h^{c^3}\ k\ \nu^c)/(3\ \nu^{c^2} - 3).$

10th row of [W]

$W(10,1) = K_u^t\ b\ h^{c^2},$
$W(10,2) = 0,$
$W(10,3) = -(K_u^t\ b\ f^t\ h^{c^2})/2,$
$W(10,4) = K_u^b\ b\ h^{c^2},$
$W(10,5) = 0,$
$W(10,6) = (K_u^b\ b\ f^b\ h^{c^2})/2,$
$W(10,7) = (2\ E^c\ b\ h^{c^3}\ k^2)/(3\ \nu^{c^2} - 3) - K_u^b\ b\ h^{c^2} - K_u^t\ b\ h^{c^2} - I_m^c\ s^2,$
$W(10,8) = (4\ G^c\ b\ i\ h^{c^3}\ k)/3,$
$W(10,9) = K_u^t\ b\ h^{c^3} - K_u^b\ b\ h^{c^3},$
$W(10,10) = (2\ E^c\ b\ h^{c^5}\ k^2)/(5\ \nu^{c^2} - 5) - (8\ G^c\ b\ h^{c^3})/3 - K_u^b\ b\ h^{c^4} - K_u^t\ b\ h^{c^4} - J_m^c\ s^2,$
$W(10,11) = K_u^t\ b\ h^{c^5} - K_u^b\ b\ h^{c^5},$
$W(10,12) = (4\ G^c\ b\ i\ h^{c^3}\ k)/3 + (2\ E^c\ b\ i\ h^{c^3}\ k\ \nu^c)/(3\ \nu^{c^2} - 3),$
$W(10,13) = 0.$

11th row of [W]

$W(11,1) = -K_u^t\ b\ h^{c^3},$
$W(11,2) = 0,$
$W(11,3) = (K_u^t\ b\ f^t\ h^{c^3})/2,$
$W(11,4) = K_u^b\ b\ h^{c^3},$
$W(11,5) = 0,$
$W(11,6) = (K_u^b\ b\ f^b\ h^{c^3})/2,$
$W(11,7) = K_u^t\ b\ h^{c^3} - K_u^b\ b\ h^{c^3},$
$W(11,8) = 2\ G^c\ b\ i\ h^{c^3}\ k,$
$W(11,9) = (2\ E^c\ b\ h^{c^5}\ k^2)/(5\ \nu^{c^2} - 5) - 2\ G^c\ b\ h^{c^3} - K_u^b\ b\ h^{c^4} - K_u^t\ b\ h^{c^4} - J_m^c\ s^2,$
$W(11,10) = K_u^t\ b\ h^{c^5} - K_u^b\ b\ h^{c^5},$
$W(11,11) = (2\ E^c\ b\ h^{c^7}\ k^2)/(7\ \nu^{c^2} - 7) - (18\ G^c\ b\ h^{c^5})/5 - K_u^b\ b\ h^{c^6} - K_u^t\ b\ h^{c^6} - K_m^c\ s^2,$
$W(11,12) = 0,$
$W(11,13) = (6\ G^c\ b\ i\ h^{c^5}\ k)/5 + (4\ E^c\ b\ i\ h^{c^5}\ k\ \nu^c)/(5\ \nu^{c^2} - 5).$

12th row of [W]

$W(12,1) = 0,$
$W(12,2) = -K_w^t\ b\ h^c,$
$W(12,3) = 0,$
$W(12,4) = 0,$
$W(12,5) = K_w^b\ b\ h^c,$
$W(12,6) = 0,$
$W(12,7) = -(2\ E^c\ b\ i\ h^c\ k\ \nu^c)/(\nu^{c^2} - 1),$
$W(12,8) = K_w^t\ b\ h^c - K_w^b\ b\ h^c,$
$W(12,9) = 0,$
$W(12,10) = -(4\ G^c\ b\ i\ h^{c^3}\ k)/3 - (2\ E^c\ b\ i\ h^{c^3}\ k\ \nu^c)/(3\ \nu^{c^2} - 3),$
$W(12,11) = 0,$
$W(12,12) = (2\ E^c\ b\ h^c)/(\nu^{c^2} - 1) - K_w^b\ b\ h^{c^2} - K_w^t\ b\ h^{c^2} - (2\ G^c\ b\ h^{c^3}\ k^2)/3 - I_m^c\ s^2,$
$W(12,13) = K_w^t\ b\ h^{c^3} - K_w^b\ b\ h^{c^3}.$

13th row of [W]

$W(13,1) = 0,$
$W(13,2) = K_w^t\ b\ h^{c^2},$
$W(13,3) = 0,$
$W(13,4) = 0,$
$W(13,5) = K_w^b\ b\ h^{c^2},$
$W(13,6) = 0,$
$W(13,7) = 0,$
$W(13,8) = -I_m^c\ s^2 - K_w^b\ b\ h^{c^2} - K_w^t\ b\ h^{c^2} - (2\ G^c\ b\ h^{c^3}\ k^2)/3,$
$W(13,9) = -(2\ G^c\ b\ i\ h^{c^3}\ k)/3 - (4\ E^c\ b\ i\ h^{c^3}\ k\ \nu^c)/(3\ \nu^{c^2} - 3),$
$W(13,10) = 0,$
$W(13,11) = -(6\ G^c\ b\ i\ h^{c^5}\ k)/5 - (4\ E^c\ b\ i\ h^{c^5}\ k\ \nu^c)/(5\ \nu^{c^2} - 5),$
$W(13,12) = K_w^t\ b\ h^{c^3} - K_w^b\ b\ h^{c^3},$
$W(13,13) = (8\ E^c\ b\ h^{c^3})/(3\ \nu^{c^2} - 3) - K_w^b\ b\ h^{c^4} - K_w^t\ b\ h^{c^4} - (2\ G^c\ b\ h^{c^5}\ k^2)/5 - J_m^c\ s^2.$

where, 'i' is an imaginary number = $\sqrt{-1}$.

References

[1] B. Hayman, Approaches to damage assessment and damage tolerance for FRP sandwich structures, J. Sandw. Struct. Mater. 9 (2007) 571–596.

[2] K. Diamanti, C. Soutis, J.M. Hodgkinson, Lamb waves for the non-destructive inspection of monolithic and sandwich composite beams, Composites 36 (2) (2005) 189–195.

[3] S. Mustapha, D. Wang, Y. Lu, Debonding detection in composite sandwich structures based on guided waves, AIAA J. 50 (8) (2012) 1697–1706.

[4] F. Song, G.L. Huang, K. Hudson, Guided wave propagation in honeycomb sandwich structures using a piezoelectric actuator/sensor system, Smart Mater. Struct. 18 (12) (2009) 125007.

[5] S. Sikdar, S. Banerjee, G. Ashish, Ultrasonic guided wave propagation and disbond identification in a honeycomb composite sandwich structure using bonded piezoelectric wafer transducers, J. Intell. Mater. Syst. Struct. 27 (3) (2016) 1767–1779.

[6] D.G. Luchinsky, V. Hafiychuk, V.N. Smelyanskiy, S. Kessler, J. Walker, J. Miller, M. Watson, Modeling wave propagation and scattering from impact damage for structural health monitoring of composite sandwich plates, Struct. Health Monit. 12 (13) (2013) 296–308.

[7] J.F. Doyle, Wave Propagation in Structures, Springer, 1997.

[8] S. Gopalakrishnan, A. Chakraborty, D.R. Mahapatra, Spectral Finite Element Method, Springer, 2007.

[9] U. Lee, Spectral Element Method in Structural Dynamics, John Wiley and Sons, 2009.

[10] P. Bonfiglio, F. Pompoli, A.T. Peplow, A.C. Nilsson, Aspects of computational vibration transmission for sandwich panels, J. Sound Vib. 303 (2007) 780–797.

[11] M.V.V.S. Murthy, K. Renji, S. Gopalakrishnan, Multi-transform based spectral element to include first order shear deformation in plates, Int. J. Mech. Sci. 96–97 (2015a) 110–120.

[12] C.N. Phan, Y. Frostig, G.A. Kardomateas, Analysis of sandwich beams with a compliant core and with in-plane rigidity—extended high-order sandwich panel theory versus elasticity, J. Appl. Mech. 79 (2012) 041001/1–041001/11.

[13] M.V.V.S. Murthy, K. Renji, S. Gopalakrishnan, A spectral element for wave propagation in honeycomb sandwich construction considering core flexibility, Compos. Struct. 127 (2015b) 28–40.

[14] I. Odessa, Y. Frostig, O. Rabinovitch, Modeling of interfacial debonding propagation in sandwich panels, Int. J. Solids Struct. 148–149 (2018) 67–78.

[15] I. Odessa, Y. Frostig, O. Rabinovitch, Dynamic interfacial debonding in sandwich panels, Composites 185 (15) (2020) 107733.

[16] M.V.V.S. Murthy, S. Gopalakrishnan, P.S. Nair, Signal wrap-around free spectral element formulation for multiply connected finite 1-d waveguides, J. Aerosp. Sci. Technol. 63 (1) (2011) 1–17.

[17] J.N. Reddy, Mechanics of Laminated Composite Plates, CRC Press, 1997.

[18] K.Y. Volokh, A. Needleman, Buckling of sandwich beams with compliant interfaces, Comput. Struct. 80 (2002) 1329–1335.

[19] D.J. Wilcox, Numerical Laplace transform inversion, Int. J. Electr. Eng. Educ. 15 (1978) 247–265.

[20] K.K. Sairajan, P.S. Nair, Design of low mass dimensionally stable composite base structure for a spacecraft, Composites 42 (2011) 280–288.

[21] L.J. Gibson, M.F. Ashby, Cellular Solids, Cambridge University Press, 1997.

[22] A.H. Meitzler, Backward-wave transmission of stress pulses in elastic cylinders and plates, J. Acoust. Soc. Am. 38 (1965) 835–842.

[23] P.L. Marston, Negative group velocity lamb waves on plates and applications to the scattering of sound by shells, J. Acoust. Soc. Am. 113 (5) (2003) 2659–2662.

[24] M. Werby, H. Uberall, The analysis and interpretation of some special properties of higher order symmetric lamb waves: The case for plates, J. Acoust. Soc. Am. 111 (6) (2002) 2686–2691.

[25] C. Schaal, A. Mal, Core–skin disbond detection in a composite sandwich panel using guided ultrasonic waves, J. Nondestruct. Eval. Diagn. Progn. Eng. Syst. 1 (2018) 011006/1–011006/8.